



Supramolecular assembly promoted synthesis of three-dimensional nitrogen doped graphene frameworks as efficient electrocatalyst for oxygen reduction reaction and methanol electrooxidation

Lei Zhao^a, Xu-Lei Sui^a, Jia-Zhan Li^a, Jing-Jia Zhang^a, Li-Mei Zhang^a, Guo-Sheng Huang^b, Zhen-Bo Wang^{a,*}

^a School of Chemistry and Chemical Engineering, Harbin Institute of Technology, No. 92 West-Da Zhi Street, Harbin, 150001 China

^b State Key Laboratory for Marine Corrosion and Protection, Luoyang Ship Material Research Institute (LSMRI), No. 149-1 Zhuzhou Road, Qingdao, 266101 China

ARTICLE INFO

Keywords:

Supramolecule
Nitrogen-doped graphene
3D hierarchical structure
Oxygen reduction reaction
Methanol oxidation reaction

ABSTRACT

Nitrogen-doped three-dimensional porous graphene frameworks (NGAs) are fabricated through a unique strategy of adopting the supramolecular assembly-assisted method with GO as building block, and supramolecular aggregate of self-assembled melamine and cyanuric acid as not only a “spacer” to suppress the re-stacking of graphene nanosheets but a self-sacrificial pore-forming agent as well as a nitrogen source leading to simultaneous N-doping. Supramolecular aggregates function as the structure-directing agent playing a vital role in generating the loose porous and free-stacking structure and guiding the formation of unique 3D architecture. The resulting metal-free NGA products possess high specific surface area, porous structure and free-stacking properties, and exhibit enhanced ORR performance in terms of positive half-wave potential which is only ~43 mV lower than that of a commercial Pt/C, four-electron-transfer process, good durability and outstanding methanol poisoning tolerance. Besides, it also performs as a good support for Pt particles. Consequently, Pt/NGA catalyst displays impressive catalytic activity and stability towards efficient methanol electrooxidation reaction. This simple and robust synthetic strategy of 3D N-doped graphene has put forward a new prospect for rational synthesis of heteroatoms doped carbon materials for sustainable energy conversion applications.

1. Introduction

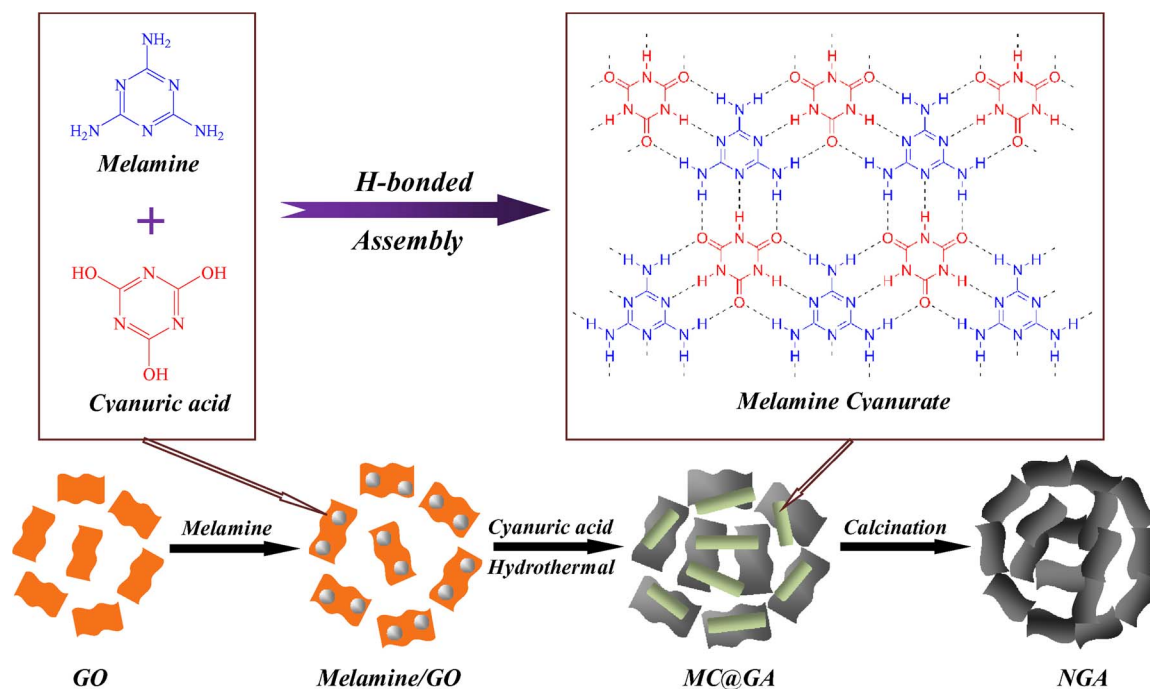
Green and efficient energy conversion technology has been considered as a promising avenue to address fossil energy exhaustion, greenhouse gases emission and environmental pollution [1]. Fuel cells in which hydrogen (fuel) oxidation and oxygen (air) reduction occurring at anode and cathode separately are just such equipment that show great potential as power source for portable devices [2,3]. However, sluggish reaction kinetics of methanol oxidation reaction (MOR) and oxygen reduction reaction (ORR) impede the process to realize its commercialization [4,5]. Pt-group precious metals are the most efficient catalysts to lower the activation energy and decrease the overpotential. Unfortunately, widespread applications of precious metals for fuel cells face the challenges of their scarcity, high cost, susceptibility to be poisoned and inferior long-term stability [6,7]. Therefore, massive efforts have been poured into research and development of low-cost and high-efficient catalysts using non-precious metals. To this end, 3d-transition metal, metal oxide, nitride, carbide, sulfide and heteroatoms

doped carbon materials have been extensively exploited for MOR and ORR [8–10].

To date, carbon materials doped with heteroatoms (e.g., B, N, S and P) or/and 3d-transition metal (e.g., Fe and Co) are regarded as impressive alternatives of Pt-based metals for ORR [11–13]. Graphene has rapidly received tremendous attention and becomes the research hotspot in the materials science field, since it was first isolated in 2004 [14]. The appealing features including large surface area, high conductivity and excellent mechanism strength render it a distinguishable catalyst candidate for fuel cell [15–17]. Nitrogen-doped graphene was deemed as promising alternative to substitute for Pt for ORR or support candidate for MOR [18]. Nitrogen-doped graphene fabricated by chemical vapor deposition is raised by Dai's group [19]. The resultant N-graphene presents superior ORR performance in terms of large steady-state catalytic current, long-time stability, and tolerance to poison effect. Zhou et al. interrogated the role of nitrogen species in catalysts by using density functional theory as well as experimental analysis and pointed out that the doping nitrogen into graphite surface will change

* Corresponding author.

E-mail address: wangzhibo@hit.edu.cn (Z.-B. Wang).



Scheme 1. The synthetic procedure of NGA materials.

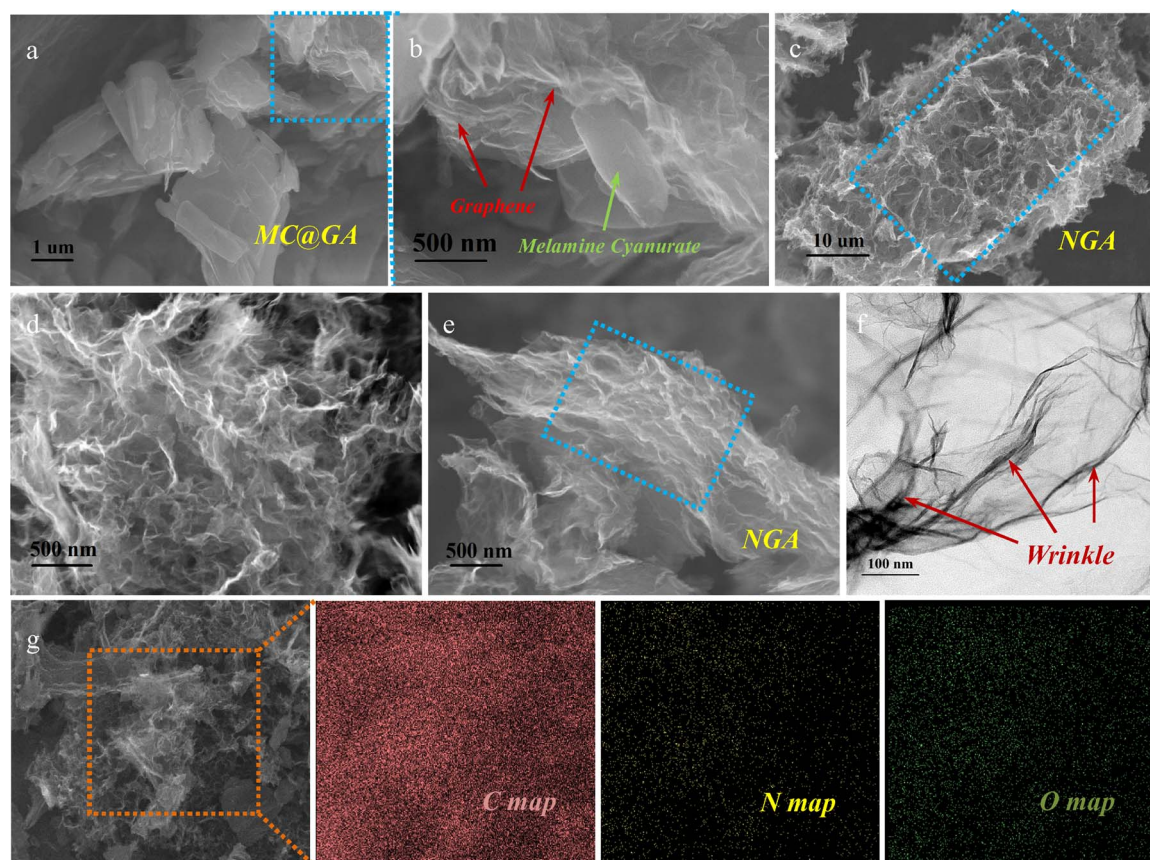


Fig. 1. SEM images of MC@GA (a,b) and NGA (c-e); TEM images of NGA (f); SEM image of NGA and the corresponding elemental mapping images for: C, N and O.

the electronic structure and modify Pt binding energy, which lead to the improved catalytic activity and stability [20]. However, the current synthetic strategies of N-doped graphene suffer from complex synthesis procedure, time-consuming, environment-polluting. Besides, thermal reduction usually leads to the inevitable stacking of graphene sheets

[21]. Therefore, it is highly desirable to achieve N-doped graphene constructed porous and free-agglomerating structure through facile, processing-simple, environment-friendly strategy.

Hydrogen-bonded supramolecular self-assembled by intermolecular hydrogen bonds among molecules have emerged as promising

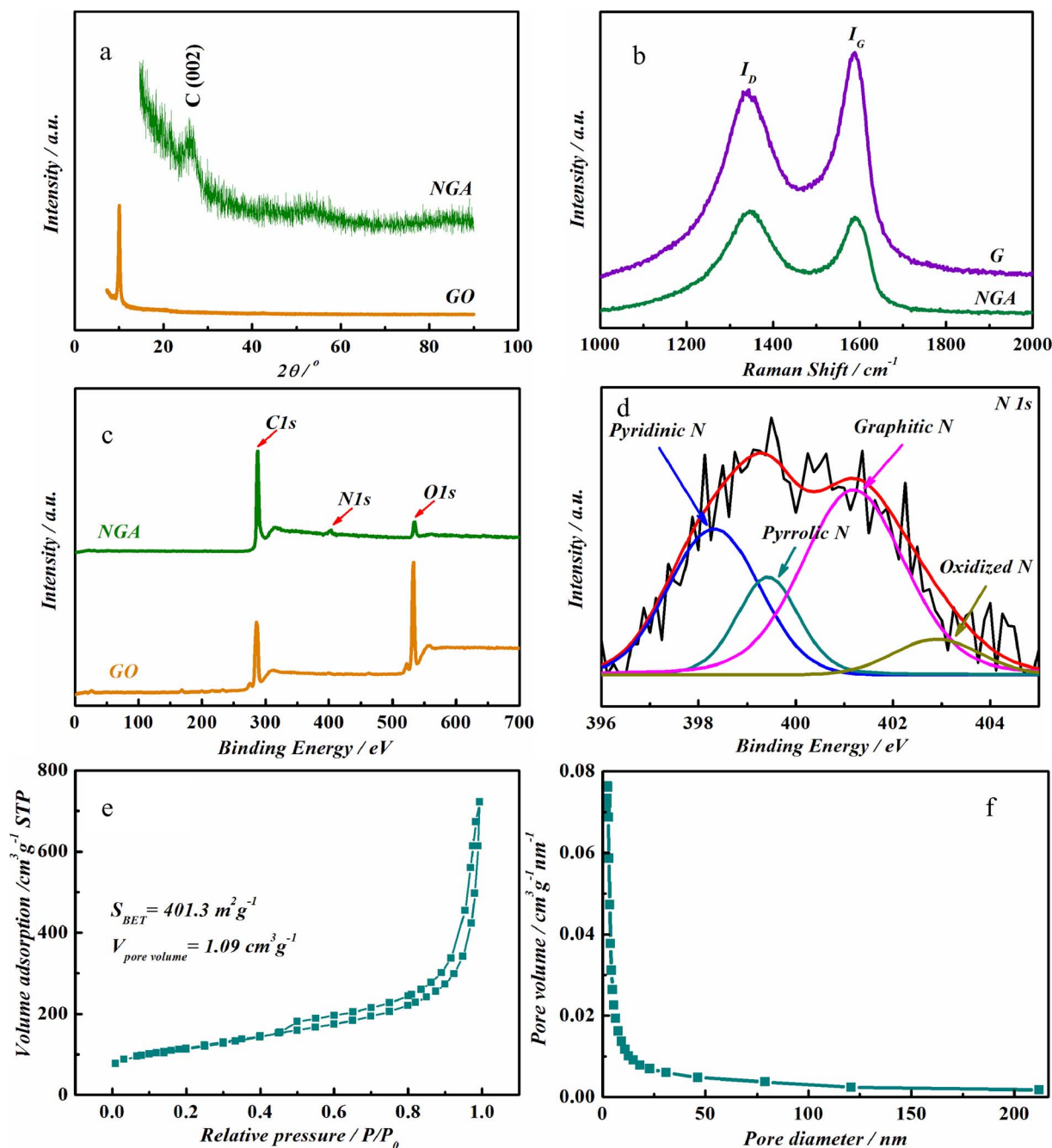


Fig. 2. XRD patterns of GO and NGA (a); Raman spectra of G, GA and NGA (b); XPS spectra of GO and NGA (c); High-resolution N 1s XPS spectra of NGA (d). Nitrogen adsorption – desorption isotherm (e) and the corresponding pore size distribution (f) of NGA.

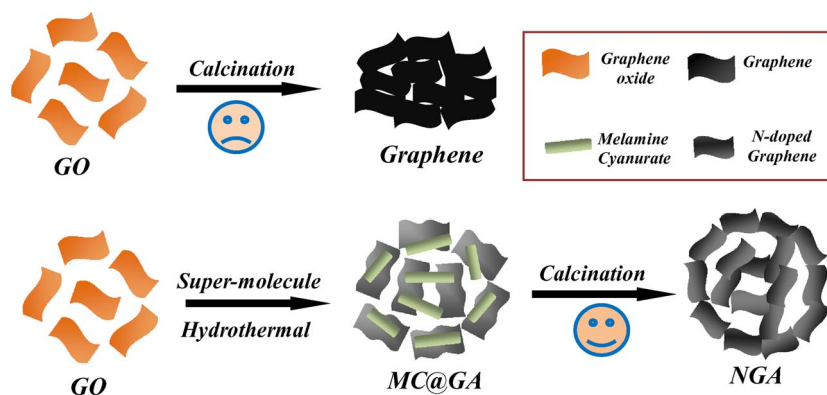
candidates for catalysis, gas sensing and photoelectric materials [22–24]. It is expected to perform as N source precursor for N doping by simple calcination process and self-sacrificial template to manufacture porous structure [25]. Herein, we propose a robust and simple method to fabricate 3D porous N-doped graphene aerogel (NGA) with GO as building block, and melamine-cyanurate supramolecule as both N source and self-sacrificial pore former. Introduction of melamine-cyanurate supermolecule can efficiently prevent the graphene sheets re-stacking, at the same time 3D hierarchical pore-rich structure and high specific surface area was achieved. The obtained NGA product exhibited efficient electrocatalytic activity for ORR in terms of positive half-wave potential, high limiting current density, good stability and superior methanol crossover tolerance. Besides, it also displayed excellent catalytic activity and stability for methanol electrooxidation

when using a support for the Pt particles. Therefore, our study opens up new avenues for facile, mass production of high-efficient heteroatoms doped carbon-based catalysts with high potential for advanced energy conversion technologies.

2. Experimental section

2.1. Fabrication of NGA samples

Graphene oxide (GO) was obtained from natural graphite powder via modified Hummers' method as Shao's work [26]. In a typical synthesis of NGA, 60 mg GO was uniformly dissolved in 30 mL deionized water under ultrasonic treatment. Then 84 mg melamine was added into the prepared GO aqueous solution with continuous stirring



Scheme 2. Schematic comparison of fabrication approaches for G and NGA.

at 80 °C and subsequently mixed with 86 mg cyanuric acid. Afterward, the above dispersion was delivered to a 50 mL Teflon-lined autoclave and maintained under hydrothermal condition at 180 °C for 6 h. After washed with ultrapure water and dried by lyophilization, the resultant product was annealed at 1000 °C for 1 h under Argon atmosphere to get the final NGA. GA was prepared in the same procedure except adding melamine and cyanuric acid. Graphene (G) was obtained by directly annealing GO in the same pyrolysis conditions.

2.2. Synthesis of Pt/NGA catalyst

Pt/3D-NGA catalyst with Pt-loading amount of 20 wt.% was fabricated via a microwave assisted polyol reduction process. In short, 20 mg synthesized NGA was thoroughly suspended into 60 mL of ethylene glycol (EG) and ultrasonicated to form homogeneous slurry. Subsequently, the calculated amount of H_2PtCl_6 -EG solution was dripped into slurry. After the NaOH-EG solution was dropwise incorporated to adjust the pH value of the suspension to 12.0, the dispersion was subjected to continuous microwave heating for 55 s. The final sample was obtained after being washed with deionized water followed by vacuum drying. Commercial 20 wt.% Pt/C was used as a benchmark to compare the electrocatalytic performance of the both catalysts.

2.3. Characterizations

Powder X-ray diffraction (XRD) was conducted on the D/max-RB diffractometer. X-ray photoelectron spectroscopy (XPS) analysis was measured a physical electronics PHI model 5700 instrument. Scanning electron microscope (SEM) and transmission electron microscope (TEM) were carried out on Hitachi S4800 and FEI Tecnai G2 F20, respectively. Raman spectra were performed on a Renishaw1000 Raman microscope. Nitrogen adsorption/desorption analysis was implemented on a QUADRASORB SI analyzer.

2.4. Electrochemical measurements

The electrochemical tests were conducted on a standard three-electrode system using CHI 650E electrochemical analysis instrument. For ORR, a rotating disk electrode (RDE) covered with prepared NGA catalysts; platinum net and Ag/AgCl (3 mol L⁻¹ KCl solution) were applied as working, counter and reference electrodes, respectively. Cyclic voltammetry (CV), linear sweep voltammetry (LSV) and chronoamperometry were executed in O₂ saturated 0.1 mol L⁻¹ KOH aqueous solution. For MOR, a glassy carbon disk electrode, platinum net and Hg/Hg₂SO₄ were employed as working, counter and reference electrodes, respectively. Electrolyte solution was changed to Ar-saturated 0.5 mol L⁻¹ H₂SO₄ aqueous solution or 0.5 mol L⁻¹ H₂SO₄ containing 0.5 mol L⁻¹ CH₃OH. All electrochemical experiments were performed

at room temperature. More detailed information about the electrode preparation process, physical characterization, and electrochemical measurements are given in the Supporting Information.

3. Results and discussions

3.1. NGA fabricated from supramolecular assembly-assisted method

3.1.1. Synthetic procedure for NGA

As shown in Scheme 1, 3D nitrogen-doped graphene aerogel (NGA) was formed through a simple two-step method. In the first step, melamine was dispersed in GO aqueous solution and stuck on the surface of GO nanosheets via π - π interaction [27]. Afterwards, cyanuric acid was mixed in the prepared solution. Supramolecular melamine-cyanurate/graphene aerogel (MC@GA) composite was obtained under hydrothermal condition. During hydrothermal process, melamine-cyanurate aggregates emerged through the hydrogen-bonding self-assembly between melamine and cyanuric acid, simultaneously, GO was reduced and self-assembled into graphene aerogel [25,28]. In addition, MC aggregate was wrapped in-between graphene sheets as “spacer” to prevent graphene sheets from severe re-stacking. Subsequently, MC@GA composite was heated at 1000 °C under Ar as protective atmosphere. During the pyrolysis process, MC component decomposed and released abundant nitrogen-containing species for in-situ doping of N into the final product [29]. The decomposition of “spacer” MC will result in internal stress, which also contributes to restraint of agglomeration of graphene sheets.

3.1.2. Physical characterization of NGA

The structure and morphology of the products are interrogated by scanning electron microscopy (SEM) and transmission electron microscopy (TEM). SEM of MC@GA shows that supramolecular melamine-cyanurate aggregates present rod-like structure in the submicrometer to micrometer range, which are wrapped within the 3D graphene framework (Fig. 1a,b). Notably, rod-like supermolecule vanishes after the thermal treatment. Fig. 1c–e confirm the 3D porous structure of the prepared NGA. The NGA demonstrates a wrinkle-like and loose-packed morphology. By contrast, the directly annealing reduced graphene, performs intensive agglomeration, implying the severe re-stacking of graphene sheets (Fig. S1) [30]. The SEM images of GA prepared in the same procedure for NGA except the addition of melamine-cyanurate aggregate are also shown in Fig. S2. Compared with the directly annealing reduced graphene, intensive agglomeration of graphene sheets is alleviated in some degree and some porous structures appear in the graphene network. However, relatively large graphene sheets constructed with stacking and cross-linked graphene layers could be still clearly seen. This phenomenon indicates the re-stacking of graphene is rather serious for G and GA. While for NGA, the crumpled graphene sheets overlapped with each other leading to the generation of

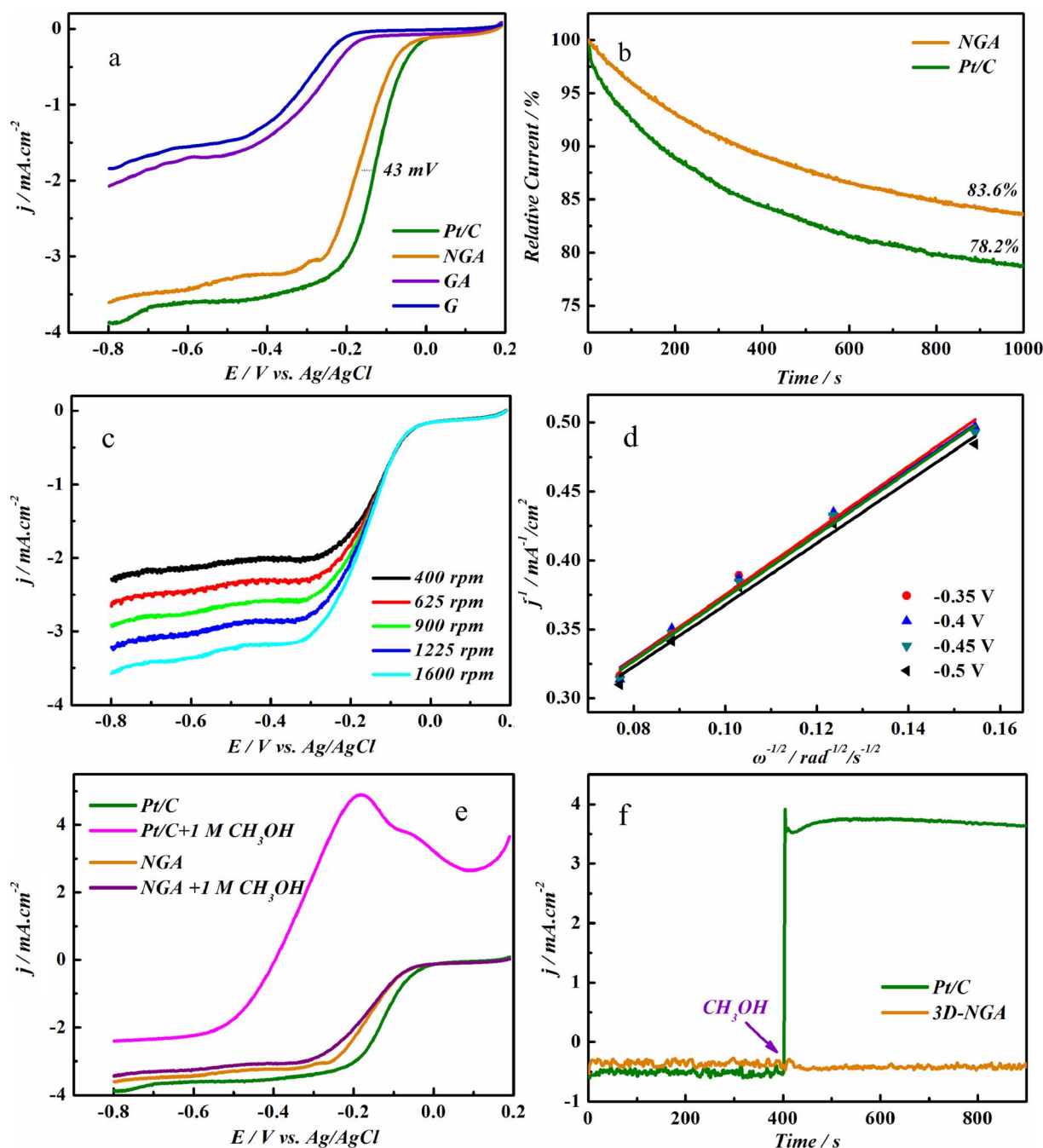


Fig. 3. LSV curves of G, GA, NGA and commercial Pt/C in O₂-saturated 0.1 mol L⁻¹ KOH electrolyte at a scanning rate of 5 mV s⁻¹ with a rotating speed of 1600 rpm (a). Chronoamperometric curves of NGA and commercial Pt/C in O₂-saturated 0.1 mol L⁻¹ KOH solution at a constant potential of -0.4 V with rotating speed of 1600 rpm (b). ORR polarization curves of NGA in O₂-saturated 0.1 mol L⁻¹ KOH solution at different rotation rates (c). the corresponding Koutecky–Levich plots at potentials of -0.35, -0.4, -0.45 and -0.5 V (d). Polarization curves of the Pt/C and NGA catalysts in O₂-saturated 0.1 mol L⁻¹ KOH solution with/without 1 mol L⁻¹ methanol at a rotation rate of 1600 rpm (e). Methanol crossover tests for NGA and commercial Pt/C conducted on RDE by injecting methanol into the electrolyte at 400 s (f).

interconnected micrometer-scaled porous structure. This structure indicates the irreversible agglomeration of graphene sheets is efficiently alleviated [31]. In addition, the volume of the NGA with the same weight is much larger than that of the GA (Fig. S3), suggesting the fluffy state of the graphene nanosheets [32]. Such interconnected porous framework could facilitate the prompt mass and electronic transfer, and also provide the sufficient active sites for Pt nanoparticles (NPs) deposition [33,34]. The free-stacking properties of NGA are further affirmed by TEM analysis. Fig. 1f shows that silk-like graphene sheets crumple and display transparent and thin, constructing 3D porous graphene framework architecture. In addition, scanning electron microscopic energy dispersive X-ray (SEM-EDX) mapping images reveal

that C, O, N atoms are found to uniformly distribute in the as-prepared NGA samples (Fig. 1g).

The structure changes of the NGA samples are characterized by X-ray diffraction (XRD) and Raman spectrum. The characterized diffraction peak in GO spectra locates at $2\theta = 10.0^\circ$, which stems from the successful insertion of oxygen-containing functional groups into the layer of the natural graphite [35]. For NGA samples, the dominating peak up-shifts to high angle (26.3°) confirming the efficient reduction of GO (Fig. 2a) [36]. Raman spectra for G, and NGA display two typical peaks, D and G bands at 1340 and 1590 cm⁻¹, respectively (Fig. 2b). The higher I_D/I_G value of NGA compared to G illustrates the existence of definite structural defects, presumably causing by the nitrogen doping

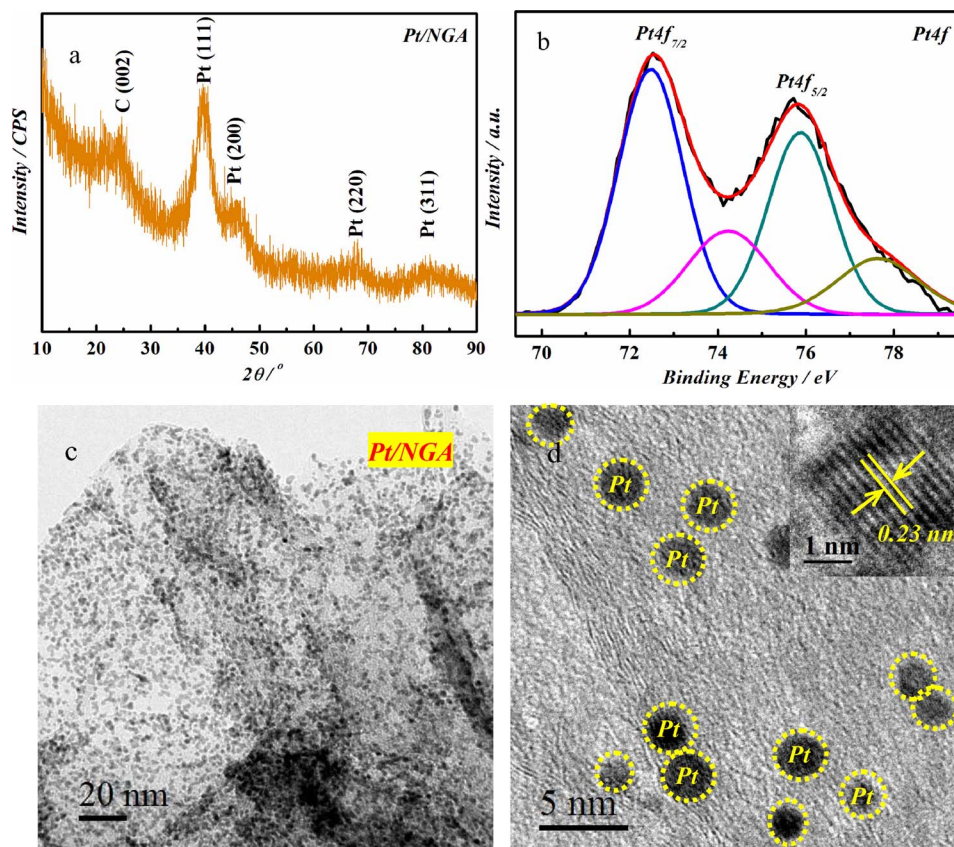


Fig. 4. XRD pattern of Pt/NGA; High-resolution Pt 4f XPS spectra of Pt/NGA (b); TEM (c) and HRTEM (d) images of Pt/NGA catalyst.

in the graphene layers [37]. The elemental composition and states on the surface of the samples are further interrogated by X-ray photoelectron spectroscopy (XPS) analysis. In Fig. 2c, the peaks corresponding to elements C, O, and N are well identified. On the basis of the XPS analysis, the N content in NGA is calculated to be 2.1 atom%. The high-resolution N 1s spectra (Fig. 2d) can be deconvoluted into four kinds of nitrogen: pyridine-like N (398.3 eV), pyrrole-like N (399.4 eV), graphite-like N (401.2 eV) and oxidized N (402.9 eV), respectively [38]. This result implies the successful incorporation of N species into the graphene framework, which can also be borne out by the emergence of C–N bonds in the C 1s spectra of the NGA samples (Fig. S4). It is found that the NGA possess high contents of pyridine-like N and graphite-like N, which have been known to be held responsible for the enhancement of ORR performance [39,40]. Nitrogen adsorption-desorption analysis was performed to further interrogate the structure of G and NGA. The relative pore structure parameters are listed in Table S1. The multiple pore distribution of NGA can be garnered from the pore-size distribution curve (Fig. 2f). It is obtained that NGA reveals a BET specific surface area (S_{BET}) of $401.3 \text{ m}^2 \text{ g}^{-1}$, much higher than that of the directly annealed GO ($49.7 \text{ m}^2 \text{ g}^{-1}$) as well as many reported graphene-based materials such as common 3D graphene ($166 \text{ m}^2 \text{ g}^{-1}$) [41], graphene nanomesh foam ($362 \text{ m}^2 \text{ g}^{-1}$) [42], etc. In addition, the corresponding cumulative pore volumes determined for NGA and G are 1.09 and $0.04 \text{ cm}^3 \text{ g}^{-1}$, respectively. The high S_{BET} and large pore volume of NGA may derive from the wrinkled and thin graphene nanosheets and the pore-rich structure.

3.1.3. Role of supramolecular aggregates

The comparison of the fabrication procedure of G and NGA is illustrated in Scheme 2. Graphene sheets obtained by directly annealing GO in the high temperature pyrolysis process stack together severely owing to the strong Van de Waals force between neighboring layers. However, in the synthesis of NGA, the overlapping and interconnecting

of graphene sheets of NGA precursors result in the formation of porous structure with the diameters ranging from submicrometer to few micrometers. Therefore, melamine-cyanurate supramolecular aggregates function as effective scaffolds wrapped in the skeletons of NGA precursors [43]. The introduction of melamine cyanurate supermolecule produces a confined space and enlarges the interlayer spacing between graphene sheets for efficiently preventing their re-stacking. During the annealing process, the decomposition of “spacer” MC supramolecular aggregates generate plentiful nitrogen containing gas creating internal stress in-between graphene sheets, which also contributes to the prevention of graphene sheets from agglomeration [25]. Consequently, supramolecular aggregates function as the structure-directing agent playing a vital role in generating the loose porous and free-stacking structure and guiding the formation of unique 3D architecture. In addition, the high specific surface area and hierarchical pore-rich structure can be achieved for NGA. The high specific surface area, large pore volume, and hierarchical pore-rich structure can expose abundantly accessible active sites for electro-catalysis and facilitate electron or mass transfer [28].

3.1.4. Electrocatalytic behavior of NGA for ORR

To gain the electrocatalytic properties of NGA for the ORR, cyclic voltammetry (CV) measurements were conducted in Ar- and O₂-saturated 0.1 mol L^{-1} KOH solutions (Fig. S5). In N₂-saturated solution, the sample shows a featureless capacitive curve, while a substantial reduction current could be discerned in O₂-saturated solution, demonstrating the electrocatalytic ability of NGA toward ORR. For the sake of further calculating the ORR performance of the prepared samples, rotating-disk electrode (RDE) tests were employed in O₂-saturated 0.1 mol L^{-1} KOH solution at a scan rate of 5 mV s^{-1} and rotating speed of 1600 rpm. Fig. 3a reveals that NGA behaves much higher ORR activity than the G and GA, in terms of on-set potential, half-wave potential and limiting diffusion current. The on-set and half-wave

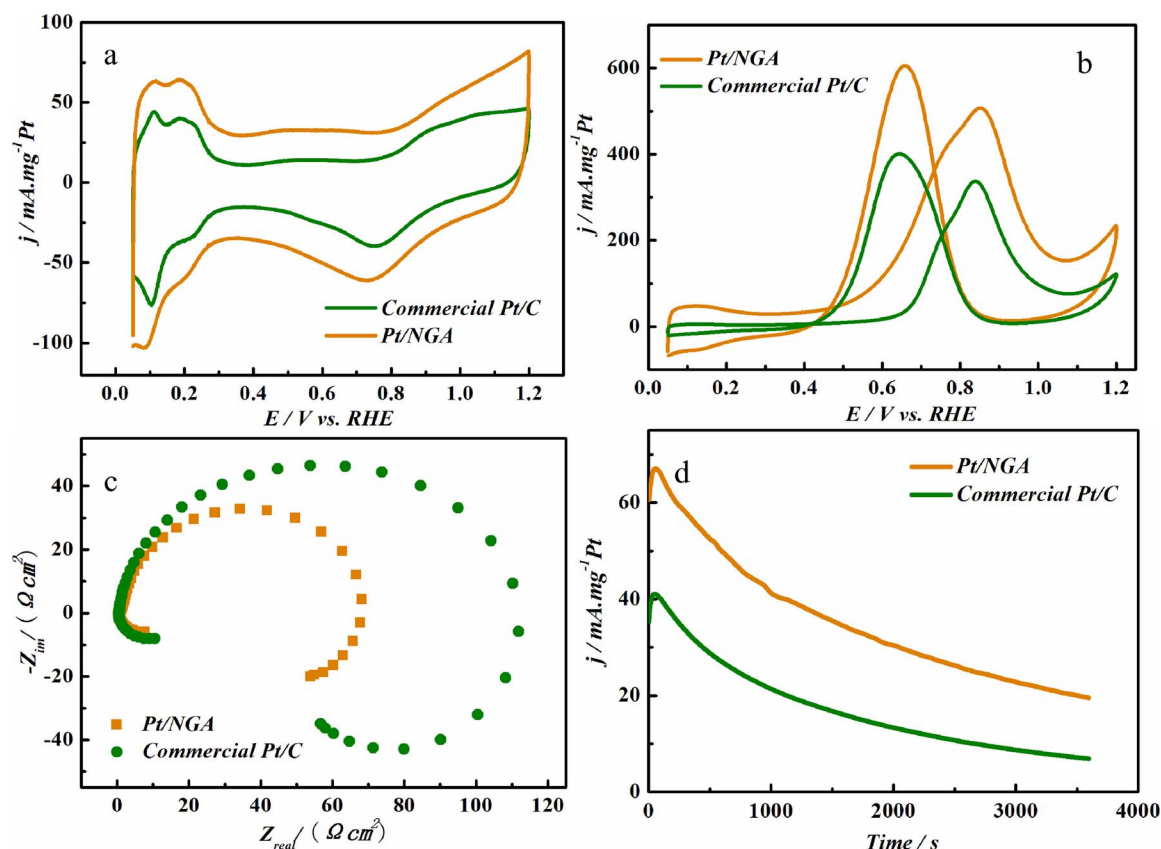


Fig. 5. CV curves of Pt/NGA and commercial Pt/C catalysts in 0.5 mol L⁻¹ H₂SO₄ (a) and in a solution of 0.5 mol L⁻¹ H₂SO₄ containing 0.5 mol L⁻¹ CH₃OH (b). Scanning rate: 50 mV s⁻¹; test temperature: 25 °C. Nyquist plots of EIS for Pt/NGA and commercial Pt/C catalysts in a solution of 0.5 mol L⁻¹ H₂SO₄ containing 0.5 mol L⁻¹ CH₃OH solution (c). Chronoamperometric curves for Pt/NGA and commercial Pt/C catalysts in a solution of 0.5 mol L⁻¹ H₂SO₄ containing 0.5 mol L⁻¹ CH₃OH at a fixed potential of 0.6 V vs. RHE (d).

potential delivered on the NGA electrodes are -0.03 and -0.17 V versus Ag/AgCl, respectively, which could be comparable to the Pt/C catalyst (0.02 and -0.13 V), while much positive than those on the G and GA. Additionally, the limiting current density on NGA is also in close proximity to that on the Pt/C catalyst, indicating the good catalytic behavior toward ORR. To further manifest the ORR mechanism on the NGA, polarization curves were recorded with different rotating rates (Fig. 3c, d). According to Koutecky–Levich (K–L) plots, the number of transferred electrons is measured to be approximately 4, suggesting the ORR on the NGA catalyst abides by a four-electron process [44].

In addition, the NGA also exhibits good methanol poison tolerance and catalytic stability toward ORR in comparison to commercial Pt/C catalyst. Chronoamperometric measurements were carried out in O₂-saturated 0.1 mol L⁻¹ KOH solution at a constant potential of -0.4 V with a rotation rate of 1600 rpm. As shown in Fig. 3b, the NGA electrode retains 84% of the initial current, which is higher than the Pt/C electrode (78%) under the same conditions, denoting better stability of the NGA than Pt/C for ORR. It has been known the methanol crossover is a big concern that will strongly deactivate the catalytic ability of ORR of Pt-based catalysts [45]. Methanol permeability in alkaline exchange membrane (AEM) fuel cell may be less of a problem compared to that in proton exchange membrane (PEM) fuel cell since hydroxyl ion transfer occurs from cathode to anode in AEM (c.f. from anode to cathode in PEM) and, by doing so, will reduce the methanol permeability [46,47]. However, due to the higher methanol concentration in anode than cathode, the permeability of methanol from anode to cathode by diffusion is spontaneous, thus the methanol crossover in AEM can not be completely eliminated [48]. Fig. 3e displays the polarization curves of the Pt/C and NGA catalysts in O₂-saturated 0.1 mol L⁻¹ KOH solution with/without 1 mol L⁻¹ methanol at a rotating speed of 1600 rpm. The

curve response on the NGA electrode presents negligible change over the addition of 1 mol L⁻¹ methanol into the electrolyte. In contrast, the Pt/C displays an obvious methanol oxidation peak, indicating severe influence of methanol on ORR process. Moreover, the NGA electrode persists nearly unchanged when the injecting of methanol at 400 s, while Pt/C exhibits an abrupt methanol oxidation current, suggesting the good methanol tolerance of the NGA for ORR [49]. This result reveals another advantage of our prepared NGA catalyst, high selectivity toward the ORR and remarkably good tolerance to methanol crossover effect, holding a high promising prospect for use as a cathode catalyst towards ORR [47].

3.2. NGA for Pt-catalyst support

3.2.1. Physical characterization of Pt/NGA

It is well known that heteroatom-doped carbon materials have been expected as effective support candidate for the electrooxidation of alcohols [50,51]. Therefore, our prepared NGA materials are also used as nano-metal Pt support to interrogate the catalytic performance for methanol electrooxidation. Pt NPs were deposited on the NGA supports through the microwave reduction process in our previous report [29]. Typical diffraction peaks of Pt [(111), (200), (220), and (311)] can be obviously discerned in the Pt/NGA spectrum (Fig. 4a), suggesting the Pt NPs exhibit face-centered cubic (fcc) structures [52]. The Pt 4f XPS of Pt/NGA hybrid manifests two states of Pt: the major one is zero-valent metallic Pt, and the other is the bivalent PtO (Fig. 4b). TEM image in Fig. 4c,d exhibit that the sphere-like Pt NPs with diameters of approximately 2 nm appear on the surface of crumpled graphene sheets, exhibiting uniform distribution and no aggregate. HRTEM investigations (inset of Fig. 4d) of sample reveal clear lattice fringes with an interplanar space of 0.23 nm, in good consistent with faced-centered

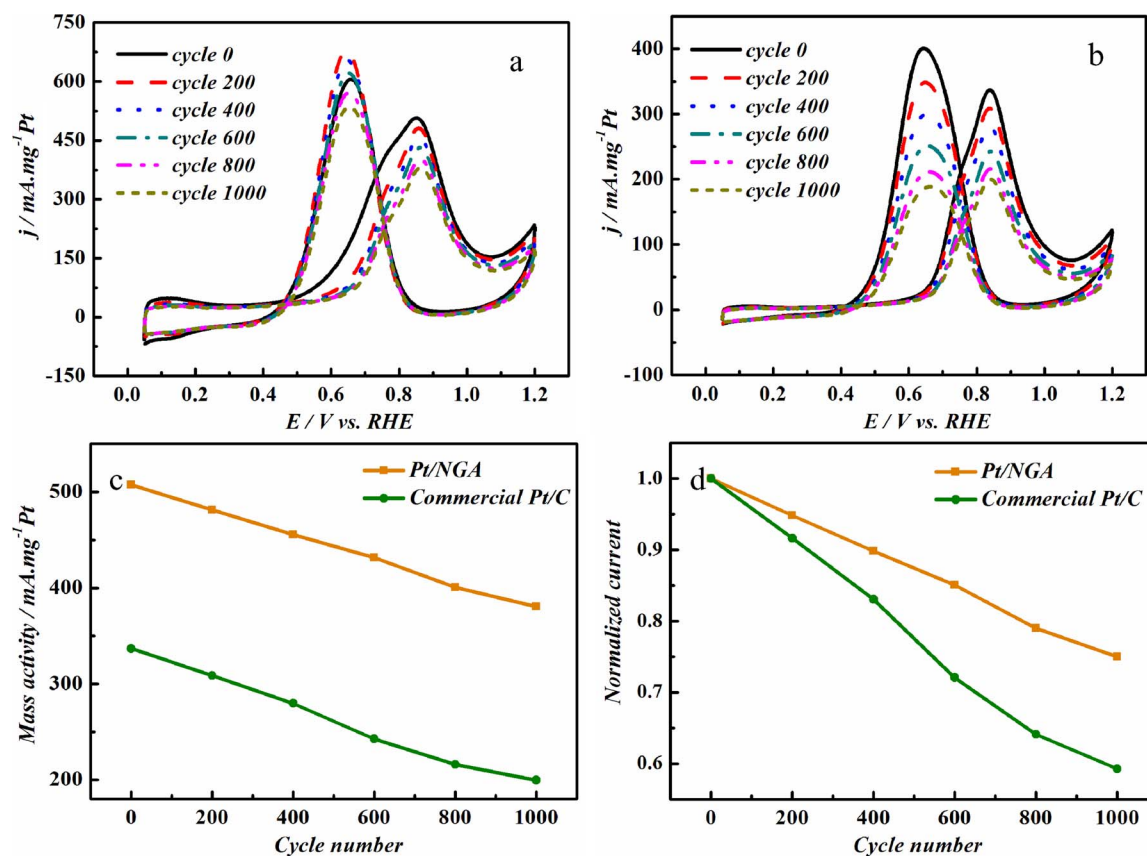


Fig. 6. CV of Pt/NGA (a) and commercial Pt/C (b) in a solution of $0.5 \text{ mol L}^{-1} \text{H}_2\text{SO}_4$ containing $0.5 \text{ mol L}^{-1} \text{CH}_3\text{OH}$ during the stability test. Scanning rate: 50 mV s^{-1} ; test temperature: 25°C . Mass activities of Pt/NGA and commercial Pt/C catalysts with cycle numbers during stability test (c). The normalization of initial forward peak current density of Pt/NGA and commercial Pt/C catalysts with cycle numbers during the stability test (d).

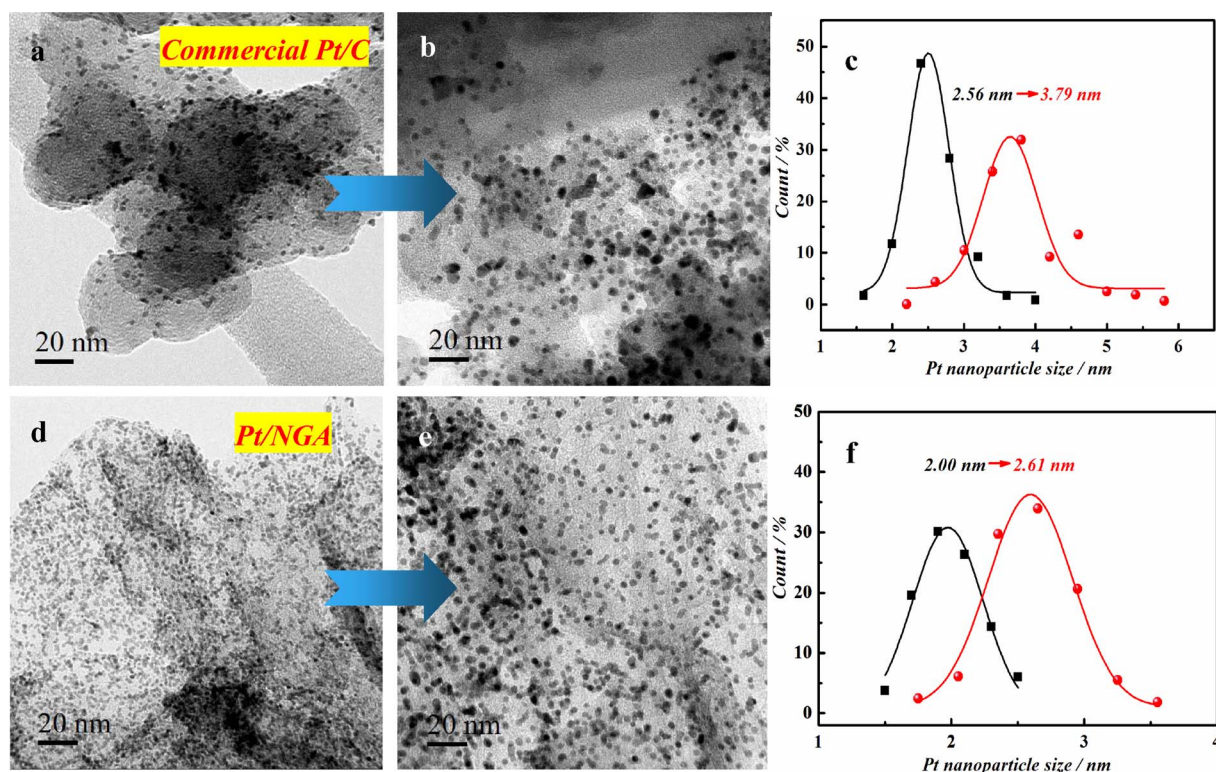


Fig. 7. TEM images with associated Pt NPs size distributions of commercial Pt/C (a, b, c) and Pt/NGA (d, e, f) catalysts before and after stability test.

cubic crystalline Pt (111) plane [53].

3.2.2. Electrocatalytic behavior of Pt/NGA for MOR

The electrochemical performance of Pt/NGA for MOR is firstly screened by cyclic voltammetry measurements in $0.5 \text{ mol L}^{-1} \text{ H}_2\text{SO}_4$ solution. Fig. 5a displays the CV curves of Pt/NGA and commercial Pt/C catalysts recorded in Ar-saturated $0.5 \text{ mol L}^{-1} \text{ H}_2\text{SO}_4$ solution. The electrochemically active surface area (ESA) of Pt/NGA determined from coulomb integral of hydrogen adsorption–desorption region is given to be $60.6 \text{ m}^2 \text{ g}^{-1}$, which is 1.16 times higher than that for commercial Pt/C ($52.4 \text{ m}^2 \text{ g}^{-1}$) [54]. This may stem from the small sizes and good dispersion of Pt NPs deposited on the 3D NGA support. The ability to catalyze methanol is further evaluated by CV measurements in $0.5 \text{ mol L}^{-1} \text{ H}_2\text{SO}_4$ containing $0.5 \text{ mol L}^{-1} \text{ CH}_3\text{OH}$ solution (Fig. 5b). The Pt/NGA electrode gives oxidation current density of 507.5 mA mg^{-1} , which is 1.5 times higher than that of commercial Pt/C (336.8 mA mg^{-1}), indicating the superior catalytic activity of the Pt/NGA than commercial Pt/C for methanol electrooxidation. Electrochemical impedance spectroscopy (EIS) is a valid means to reveal the details about the charge transfer resistance (R_{ct}) [55,56]. Fig. 5c delivers that the corresponding R_{ct} for Pt/NGA is much smaller than that for commercial Pt/C at the investigated potential, indicating that the methanol electrooxidation on Pt/NGA is more favorable than on commercial Pt/C catalyst, which agree well with the ESA and CV analyses.

Chronoamperometric measurements were employed to further scrutinize the stability of the Pt/NGA catalysts in $0.5 \text{ mol L}^{-1} \text{ H}_2\text{SO}_4$ containing $0.5 \text{ mol L}^{-1} \text{ CH}_3\text{OH}$ solution at a constant potential of 0.6 V (Fig. 5d). The current densities on both the samples decrease gradually over the chronoamperometric measurement. However, the Pt/NGA electrode presents a lower current deterioration than that on commercial Pt/C throughout the entire testing process and the final current value on Pt/NGA is approximately 3 times higher than on commercial Pt/C. These above findings manifest that the Pt/NGA exhibit much better stability compared to commercial Pt/C in acid medium. The long-time stability of catalyst is scrutinized by consecutive CVs measurement [57]. It can be observed from Figs. 6a and b, the forward current densities on both the electrodes decline gradually along with the continuous scan. After 1000 CV cycles ($0.05\text{--}1.2 \text{ V}$ vs. RHE), the normalization of initial forward peak current density of Pt/NGA loses $\sim 25\%$, whereas that of commercial Pt/C drops 40% of its initial value (Fig. 6d). It is also notable that the current density on Pt/NGA is much higher than that on commercial Pt/C all through the whole stability test. TEM images with associated Pt NPs size distributions of commercial Pt/C and Pt/NGA catalysts before and after stability measurements are presented in Fig. 7. In line with the consecutive CVs measurement responds, the particle sizes of the Pt NPs for both the two catalysts grow after 1000 CV cycles, in good agreement with their gradually decreased current densities. On the basis of TEM analysis, it could distinctly be discerned that the average sizes of Pt NPs on commercial Pt/C and Pt/NGA grow to 3.79 nm and 2.61 nm , rising by 48.0% and 30.5% , in comparison with 2.56 nm and 2.00 nm before stability test, respectively. Impressively, the particle size of commercial Pt/C displays a much broader dispersion than that on Pt/NGA after stability test. In addition, dramatic aggregation occurs to the Pt NPs on commercial Pt/C catalyst after the stability test, while it appears to a less extent regarding to Pt/NGA sample. The stability test and TEM results suggest that Pt/NGA catalyst is pretty stable during potential cycling, therefore, our prepared N-doped graphene aerogel is quite appropriate to serve as support for Pt-based catalyst toward methanol electrooxidation.

4. Conclusions

In conclusion, we have put forward a supramolecular assembly approach to three-dimensional porous graphene frameworks by hydrothermal treating of melamine-cyanurate (MC) supramolecular in the presence of GO, followed by pyrolysis treatment. Supramolecular MC

performs as both the nitrogen source and self-sacrificial pore former. The obtained NGA product presents high specific surface area, porous structure and free-stacking properties. NGA exhibits comparable ORR catalytic activity positive half-wave potential which is only $\sim 43 \text{ mV}$ lower than that of a commercial Pt/C, four-electron-transfer process and excellent stability and methanol poison tolerance. Besides, it also displays impressive catalytic activity and stability for methanol electrooxidation when using a support for the Pt particles. This work brings forward a novel avenue for design and fabrication of heteroatoms doped graphene materials for fuel cell applications.

Acknowledgment

This research is financially supported by the National Natural Science Foundation of China (Grant No. 21273058 and 21673064), China postdoctoral science foundation (Grant No. 2014T70350), Research Fund of State Key Laboratory for Marine Corrosion and Protection of Luoyang Ship Material Research Institute (No. KF160410) and HIT Environment and Ecology Innovation Special Funds (No. HSCJ201620).

Appendix A. Supplementary data

Supplementary material related to this article can be found, in the online version, at doi:<https://doi.org/10.1016/j.apcatb.2018.03.020>.

References

- [1] M.K. Debe, *Nature* 486 (2012) 43–51.
- [2] Y. Lu, S. Du, R. Steinberger-Wilckens, *Appl. Catal. B* 199 (2016) 292–314.
- [3] Q. Li, R. Cao, J. Cho, G. Wu, *Adv. Energy Mater.* 4 (2014) n/a–n/a.
- [4] J.N. Tiwari, R.N. Tiwari, G. Singh, K.S. Kim, *Nano Energy* 2 (2013) 553–578.
- [5] M.-C. Tsai, T.-T. Nguyen, N.G. Akalework, C.-J. Pan, J. Rick, Y.-F. Liao, W.-N. Su, B.-J. Hwang, *ACS Catal.* 6 (2016) 6551–6559.
- [6] L. Chen, R. Du, J. Zhu, Y. Mao, C. Xue, N. Zhang, Y. Hou, J. Zhang, T. Yi, *Small* 11 (2015) 1423–1429.
- [7] S. Guo, S. Zhang, S. Sun, *Angew. Chem. Int. Ed.* 52 (2013) 8526–8544.
- [8] Y.-J. Wang, D.P. Wilkinson, J. Zhang, *Chem. Rev.* 111 (2011) 7625–7651.
- [9] D.D. Vaughn II, J. Araujo, P. Meduri, J.F. Callejas, M.A. Hickner, R.E. Schaak, *Chem. Mater.* 26 (2014) 6226–6232.
- [10] Z.-H. Sheng, L. Shao, J.-J. Chen, W.-J. Bao, F.-B. Wang, X.-H. Xia, *ACS Nano* 5 (2011) 4350–4358.
- [11] W. Gu, L. Hu, W. Hong, X. Jia, J. Li, E. Wang, *Chem. Sci.* 7 (2016) 4167–4173.
- [12] Z. Zhang, K.L. More, K. Sun, Z. Wu, W. Li, *Chem. Mater.* 23 (2011) 1570–1577.
- [13] S. Zhang, A. Ikoma, K. Ueno, Z. Chen, K. Dokko, M. Watanabe, *ChemSuschem* 8 (2015) 1608–1617.
- [14] K. Novoselov, A.K. Geim, S. Morozov, D. Jiang, M. Katsnelson, I. Grigorieva, S. Dubonos, A. Firsov, *Nature* 438 (2005) 197–200.
- [15] B. Xia, Y. Yan, X. Wang, X.W. Lou, *Mater. Horiz.* 1 (2014) 379–399.
- [16] X. Huang, Z. Yin, S. Wu, X. Qi, Q. He, Q. Zhang, Q. Yan, F. Boey, H. Zhang, *Small* 7 (2011) 1876–1902.
- [17] H. Chang, H. Wu, *Adv. Funct. Mater.* 23 (2013) 1984–1997.
- [18] L. Lai, J.R. Potts, D. Zhan, L. Wang, C.K. Poh, C. Tang, H. Gong, Z. Shen, J. Lin, R.S. Ruoff, *Energy Environ. Sci.* 5 (2012) 7936–7942.
- [19] L. Qu, Y. Liu, J.-B. Baek, L. Dai, *ACS Nano* 4 (2010) 1321–1326.
- [20] Y. Zhou, T. Holme, J. Berry, T.R. Ohno, D. Ginley, R. O'Hayre, *J. Phys. Chem. C* 114 (2010) 506–515.
- [21] Y. Zhao, J. Liu, Y. Hu, H. Cheng, C. Hu, C. Jiang, L. Jiang, A. Cao, L. Qu, *Adv. Mater.* 25 (2013) 591–595.
- [22] X.-Z. Luo, X.-J. Jia, J.-H. Deng, J.-L. Zhong, H.-J. Liu, K.-J. Wang, D.-C. Zhong, *J. Am. Chem. Soc.* 135 (2013) 11684–11687.
- [23] P. Li, Y. He, H.D. Arman, R. Krishna, H. Wang, L. Weng, B. Chen, *Chem. Commun.* 50 (2014) 13081–13084.
- [24] J. Zhang, L. Qu, G. Shi, J. Liu, J. Chen, L. Dai, *Angew. Chem.* 128 (2016) 2270–2274.
- [25] W. Ai, J. Jiang, J. Zhu, Z. Fan, Y. Wang, H. Zhang, W. Huang, T. Yu, *Adv. Energy Mater.* 5 (2015) n/a–n/a.
- [26] Y. Shao, J. Wang, M. Engelhard, C. Wang, Y. Lin, *J. Mater. Chem.* 20 (2010) 743–748.
- [27] Q. Xiang, J. Yu, M. Jaroniec, *Chem. Soc. Rev.* 41 (2012) 782–796.
- [28] C. Hu, H. Cheng, Y. Zhao, Y. Hu, Y. Liu, L. Dai, L. Qu, *Adv. Mater.* 24 (2012) 5493–5498.
- [29] L. Zhao, X.-L. Sui, J.-L. Li, J.-J. Zhang, L.-M. Zhang, Z.-B. Wang, *ACS Appl. Mat. Interfaces* 8 (2016) 16026–16034.
- [30] D. He, K. Cheng, T. Peng, M. Pan, S. Mu, *J. Mater. Chem. A* 1 (2013) 2126–2132.
- [31] Y. Qin, L. Chao, J. Yuan, Y. Liu, F. Chu, Y. Kong, Y. Tao, M. Liu, *Chem. Commun.* 52 (2016) 382–385.

- [32] Y.-N. Hou, Z. Zhao, Z. Yu, Y. Tang, X. Wang, J. Qiu, Chem. Commun. 53 (2017) 7840–7843.
- [33] T. Sun, Z. Zhang, J. Xiao, C. Chen, F. Xiao, S. Wang, Y. Liu, Sci. Rep. 3 (2013) 2527.
- [34] S. Zhao, H. Yin, L. Du, G. Yin, Z. Tang, S. Liu, J. Mater. Chem. A 2 (2014) 3719–3724.
- [35] Q. Huang, F. Tao, L. Zou, T. Yuan, Z. Zou, H. Zhang, X. Zhang, H. Yang, Electrochim. Acta. 152 (2015) 140–145.
- [36] Y. Qu, Y. Gao, L. Wang, J. Rao, G. Yin, Chem.–A Eur. J. 22 (2016) 193–198.
- [37] Y. Xue, J. Liu, H. Chen, R. Wang, D. Li, J. Qu, L. Dai, Angew. Chem. Int. Ed. 51 (2012) 12124–12127.
- [38] L. Zhao, X.-L. Sui, J.-L. Li, J.-J. Zhang, L.-M. Zhang, Z.-B. Wang, Catal. Commun. 86 (2016) 46–50.
- [39] D. Geng, Y. Chen, Y. Chen, Y. Li, R. Li, X. Sun, S. Ye, S. Knights, Energy Environ. Sci. 4 (2011) 760–764.
- [40] D. Zhu, L. Li, J. Cai, M. Jiang, J. Qi, X. Zhao, Carbon 79 (2014) 544–553.
- [41] L. Zhang, G. Shi, J. Phys. Chem. C 115 (2011) 17206–17212.
- [42] Y. Zhao, C. Hu, L. Song, L. Wang, G. Shi, L. Dai, L. Qu, Energy Environ. Sci. 7 (2014) 1913–1918.
- [43] C. Zhao, C. Yu, S. Liu, J. Yang, X. Fan, H. Huang, J. Qiu, Adv. Funct. Mater. 25 (2015) 6913–6920.
- [44] H. Yan, M. Meng, L. Wang, A. Wu, C. Tian, L. Zhao, H. Fu, Nano Res. 9 (2016) 329–343.
- [45] H.J. Cui, H.M. Yu, J.F. Zheng, Z.J. Wang, Y.Y. Zhu, S.P. Jia, J. Jia, Z.P. Zhu, Nanoscale 8 (2016) 2795–2803.
- [46] Y. Xiong, Q.-L. Liu, A.M. Zhu, S.M. Huang, Q.H. Zeng, J. Power Sources 186 (2009) 328–333.
- [47] D.-S. Yang, D. Bhattacharjya, S. Inamdar, J. Park, J.-S. Yu, J. Am. Chem. Soc. 134 (2012) 16127–16130.
- [48] K. Scott, E. Yu, G. Vlachogiannopoulos, M. Shivare, N. Duteanu, J. Power Sources 175 (2008) 452–457.
- [49] L. Shen, T. Sun, O. Zhuo, R. Che, D. Li, Y. Ji, Y. Bu, Q. Wu, L. Yang, Q. Chen, X. Wang, Z. Hu, ACS Appl. Mat. Interfaces 8 (2016) 16664–16669.
- [50] C. Galeano, J.C. Meier, M. Soorholtz, H. Bongard, C. Baldizzone, K.J.J. Mayrhofer, F. Schüth, Acs Catal. 4 (2014) 3856–3868.
- [51] J. Zhang, L. Ma, M. Gan, F. Yang, S. Fu, X. Li, J. Power Sources 288 (2015) 42–52.
- [52] C. Kok Poh, S. Hua Lim, Z. Tian, L. Lai, Y. Ping Feng, Z. Shen, J. Lin, Nano Energy 2 (2013) 28–39.
- [53] L. Zhao, Z.-B. Wang, J. Liu, J.-J. Zhang, X.-L. Sui, L.-M. Zhang, D.-M. Gu, J. Power Sources 279 (2015) 210–217.
- [54] R.-X. Wang, J.-J. Fan, Y.-J. Fan, J.-P. Zhong, L. Wang, S.-G. Sun, X.-C. Shen, Nanoscale 6 (2014) 14999–15007.
- [55] M. Shao, F. Ning, J. Zhao, M. Wei, D.G. Evans, X. Duan, Adv. Funct. Mater. 23 (2013) 3513–3518.
- [56] J. He, Y. Chen, W. Lv, K. Wen, C. Xu, W. Zhang, W. Qin, W. He, ACS Energy Lett. 1 (2016) 820–826.
- [57] Y.Y. Chu, Z.B. Wang, Z.Z. Jiang, D.M. Gu, G.P. Yin, Adv. Mater. 23 (2011) 3100–3104.